Scaling of mouse somitogenesis by coupling of cell cycle to segmentation clock oscillations

Marek J. van Oostrom[1], Yuting I. Li[2,3], Wilke H. M. Meijer[1], Tomas E. J. C. Noordzij[1], Charis Fountas[1,$], Erika Timmers[1], Jeroen Korving[1], Wouter M. Thomas[1], Benjamin D. Simons[2,4,5] and Katharina F. Sonnen[1,*]

[1]Hubrecht Institute-KNAW (Royal Netherlands Academy of Arts and Sciences), University Medical Center Utrecht, Utrecht, The Netherlands

[2]Department of Applied Mathematics and Theoretical Physics, Centre for Mathematical Sciences, University of Cambridge, Wilberforce Road, Cambridge CB3 0WA, UK

[3]Institute of Science and Technology Austria (ISTA), 3400 Klosterneuburg, Austria

[4]Gurdon Institute, University of Cambridge, Tennis Court Road, Cambridge, CB2 1QN, UK

[5]Cambridge Stem Cell Institute, Jeffrey Cheah Biomedical Centre, University of Cambridge, Cambridge, CB2 0AW, UK

[$]present address: Division of Gene Regulation, the Netherlands Cancer Institute, Oncode Institute, Plesmanlaan 121, 1066CX Amsterdam, the Netherlands

*Correspondence: k.sonnen@hubrecht.eu

Somitogenesis is the periodic segmentation of a continuously growing tissue in vertebrate embryos[1]. Timing and spacing of somitogenesis is regulated by the segmentation clock, oscillations in Notch, Wnt and FGF signalling in mice, and FGF and Wnt morphogen gradients[2-4]. The size of nascent somites scales with the size of the unsegmented region, the presomitic mesoderm (PSM), over developmental time and upon experimental perturbation of PSM size[5-7]. Here, we addressed how scaling is ensured in the developing mouse embryo. We found that the entire oscillating presomitic mesoderm proliferates. Quantifying the dynamics of signalling and cell cycle progression in single cells, we detected a correlation between the two. Using a

microfluidics-based entrainment approach, we showed that signalling oscillations and cell cycle are coupled, likely via periodic induction of S phase-inducing Cyclins. An updated theoretical somitogenesis model incorporating this coupling suggests that this correlation ensures uniform PSM growth and uniform dilution of morphogen gradients by cell divisions, thereby directly affecting somite formation. Indeed, when blocking cell proliferation, gradient spreading and somite formation as well as somite scaling are impaired. Our data suggests a mechanism by which coupling signalling oscillations to cell proliferation ensures formation of properly sized somites and scaling of somite size.

Main

Somitogenesis is highly reproducible between individual animals. Cells starting in the posterior tip of the embryo tail traverse the PSM bilaterally to the neural tube, until differentiation and somite formation is induced in anterior PSM[1]. Imbalance between growth and segmentation can lead to premature or delayed arrest in somite formation, improperly sized somites or asymmetries between left and right[6-8]. Scaling of somitogenesis, the relative adjustment of somite size to PSM size, occurs during mouse development when PSM size first increases until embryonic day (E)9.5 and then decreases until the somitogenesis terminates[5]. Moreover, experimentally decreasing PSM size results in the formation of smaller somites[6,7]. The potential involvement of cell proliferation in somitogenesis has been a subject of discussion and controversy. Described as the main contributor to PSM growth[9-11], cell cycle inhibition does not interfere with segmentation clock oscillations in 2D *in vitro* culture models of human somitogenesis[12]. In zebrafish embryos, absence of proliferation impairs proper somite formation and has been described as a source of noise for the segmentation clock[5,8,13-15]. A link between segmentation clock and cell division has been suggested[14-16], but not formally shown.

Results

Cell cycle dynamics along the PSM

To understand the role of cell proliferation in somitogenesis, we first characterized cell cycle dynamics in uncultured mouse embryo tails. Immunostaining for the cell cycle marker Ki67 implied that all PSM cells were actively cycling (Fig. 1A). We then used flow cytometry to determine distribution into the four cell cycle phases: G1, S (when DNA replication occurs), G2 and M phase (when cell division occurs). We specifically analysed Tbx6-positive PSM cells and found that most cells were in S phase (60.4%), while fewer were either in G1 (22.7%) or G2/M phase (16.9%, Fig. 1B, Fig. S1). Previously, we have found that cell proliferation occurs in the entire PSM[10]. To quantify this precisely along the anteroposterior (AP) axis, we performed immunostaining using the mitotic cell marker pHH3 in mouse embryonic tails transversally sectioned from posterior to anterior (Fig. 1C-E, Fig. S2). We confirmed that cells divided within the tailbud, PSM and somite region of the tail (Fig. 1E). Furthermore, there was a slight increase in the percentage of late mitotic cells within the first two forming somites compared to the PSM.

Next, we quantified the proliferation rate in embryo tails using sequential pulse labelling with thymidine analogues 5-Ethynyl-2′-deoxyuridine (EdU) followed by 5-Bromo-2′-deoxyuridine (BrdU) 1 h later and quantified cell cycle timing in similarly transversally sectioned tails[17,18] (Fig. 1C,F-H, Fig. S3). Cell cycle length was quantified using the formula $Cell\ cycle\ length = \frac{Total\ cell\ number \times 1\ h}{EdU^{+}BrdU^{-}cell\ number}$. The differentially labelled cell fractions allowed us to quantify cell cycle and S-phase duration. Cell cycle duration within the tailbud and PSM was approximately 14 hours (Fig. 1H, Fig. S3D) and S phase duration 10 hours (Fig. S3E-G). With a segmentation clock period of 2.7 hours this indicates proliferation results in tissue size doubling in around 5 segmentation cycles.

Within the first two somites, the overall cell cycle length was decreased relative to the PSM, which is in line with the increase in mitotic cells (Fig. 1E,H). Interestingly, variability in cell cycle duration was higher in somites, hinting at tighter cell cycle control in the PSM than in differentiating somites. Thus, cells divide along the whole AP axis of the PSM, suggesting constant stretching of the entire PSM. This contrasts with a model in which cells are added in the posterior PSM, while segmentation occurs in the anterior.

101

102 **Quantification of cell cycle dynamics in real-time**

103 We subsequently determined real-time cell cycle dynamics in the
104 growing mouse embryo. To this end, we cultured E10.5 embryo tails expressing
105 the inducible Fucci2 cell cycle G1 reporter R26R-mCherry-hCdt1(30/120)[19]
106 (Fucci2-Cdt1) *ex vivo* and quantified reporter expression in single cells over
107 time. To make this possible, we established single-cell tracking in the growing
108 embryonic tail by combining mosaic labelling with light-sheet microscopy (Fig.
109 1I-N, Fig. S4A-C). We combined the inducible Fucci2 reporter[19] with the
110 inducible nuclear marker R26R-iRFPnucmem[20] (iRFPnucmem) and induced
111 sparse labelling with injections of low concentrations of Tamoxifen in the
112 mother. Cell cycle duration was on average 13.6 hr, corresponding to the cell
113 cycle timing *in vivo* (Fig. 1H), and cells spent on average 4.4 hr in G1 phase
114 (Fig. 1N). Notably, we did not detect changes in cell density despite cell
115 divisions over 24 hr of real-time imaging (Fig. S4D,E), indicating that cells grow
116 and divide during tissue growth.

117 To determine if there was any spatiotemporal regulation of cell cycle
118 progression in the PSM, we analysed the spatial organization of cells double-
119 positive for both the Fucci reporters mKuzabiraOrange2-Cdt1 (Fucci1-Cdt1)
120 and mAzabiGreen-hGem(1/110) (Fucci1-Gem), which specifically marks cells
121 at the G1-S transition[21]. Notably, the spatial pattern of double-positive cells
122 differed between independent embryo tails with some having no double-
123 positive cells in the PSM and others having stripes at different locations
124 throughout the PSM (Fig. 1O, Fig. S4F). This behaviour is analogous to fixed
125 images of cyclic segmentation clock genes that show different expression
126 patterns in different embryos[22,23]. This implies that there might be a
127 spatiotemporal organization of cell cycle entry in the PSM.

128

129 **Segmentation clock and cell cycle are correlated**

130 To investigate if there was a correlation between cell proliferation and
131 segmentation clock oscillations, we simultaneously quantified cell cycle
132 progression using the inducible nuclear marker R26R-H2B-mCherry[24] and the
133 segmentation clock using the reporter Achilles-Hes7[25] (Fig. 2A-D, Fig. S5).
134 Based on the nuclear marker, we tracked single cells, aligned tracks to the time

135 of cell division and analysed Hes7 expression (Fig. 2C). Immediately after cell
136 division, daughter cells of a given mother tended to oscillate more in-phase than
137 several hours after division (Fig. S5C). Moreover, we did not detect a
138 preferential division axis along the anteroposterior axis (Fig. S5D). Interestingly,
139 we found that the Hes7 oscillation phase before division was not randomly
140 distributed. At the point of cell division, there was a sudden drop in Hes7 signal
141 presumably due to nuclear envelope breakdown. After division, individual cells
142 immediately showed Hes7 oscillations again (Fig. S5A), but aligned tracks
143 showed no synchronized behaviour for approximately 4 hours, when cells
144 started to resynchronize again (Fig. 2C,D, Fig. S5E). This timeframe of non-
145 synchronization roughly corresponds to the time cells spent in G1 phase of the
146 cell cycle (Fig. 1N).

147 The G1 restriction point is a point of no return, after which the cell cycle
148 can run autonomously, even though later restriction points can prevent cell
149 cycle progression to ensure fidelity of cell division[26]. We therefore addressed
150 whether segmentation clock oscillations were correlated with G1-S transition.
151 To this end, we combined Achilles-Hes7 with Fucci2-Cdt1 and iRFPnucmem
152 (Fig. 2E-G, Fig. S6A-D) and quantified expression in single cells of *ex vivo*
153 cultured embryo tails after induction of mosaic labelling. When analysing the
154 instantaneous period of Hes7 oscillations along the posterior-anterior PSM
155 axis, we detected an increase in period towards the anterior (Fig. S7A),
156 consistent with an oscillation period gradient[27]. We then separated cell tracks
157 into their respective cell cycle phase cells, based on Fucci2-Cdt1 reporter
158 expression. In posterior PSM, cells in G1 had a higher oscillation period than
159 cells in other cell cycle phases (Fig. S7B,C). Moreover, the period gradient was
160 less clear in G1 than in S/G2/M phase cells. Also, when directly comparing all
161 cells in G1 to all cells in S/G2/M phase, independent of the location in the PSM,
162 we detected a slightly higher period in S/G2/M phase cells (Fig. S7D). This
163 indicates that oscillation parameters change with anteroposterior position in the
164 PSM and cell cycle phase suggesting an effect of cell proliferation on the
165 segmentation clock[14,28].

166 We then addressed a potential correlation between Hes7 oscillations
167 and G1-S transition. When aligning all tracks to the point of G1-S transition,
168 defined as the peak in Fucci2-Cdt1 signal (Fig. 1L), we did not observe any

169 preferred phase of Hes7 oscillations (Fig. 2G, Fig. S6E,F). In mice, the
170 segmentation clock consists of oscillations in Notch, Wnt and FGF signalling.
171 We have previously shown that the phase-relationship between Wnt and Notch
172 signalling changed along the posterior-anterior axis of the PSM from out-of-
173 phase in the posterior to in-phase in the anterior[29], corresponding to a 1π shift
174 in phase-relationship. If a corresponding shift in phase-relationship was present
175 for cell cycle and Hes7 oscillations, any correlation would be masked when
176 analysing the average signal. We therefore separated tracks into cells residing
177 in the posterior and anterior PSM and analysed the correlation of Fucci2-Cdt1
178 and Hes7 dynamics. Interestingly, we found that in both regions proliferation
179 and the segmentation clock were correlated (Fig. 2G, Fig. S6E,F). In posterior
180 PSM, the phase of Hes7 oscillations was at ~1.3π at G1-S transition, while it
181 was at ~0.4π in anterior PSM. This corresponded to a change in phase-
182 relationship between Notch oscillations and cell cycle of ~0.9π between
183 posterior and anterior PSM. This indirectly indicated that cell cycle progression
184 correlated with Wnt-signalling oscillations in the PSM.
185 While the cell cycle in a single cell takes approx. 14 hr, at the population
186 level we observed faster dynamics in the Fucci2-Cdt1 reporter: When
187 quantifying small regions containing approximately 10-15 cells, we observed
188 oscillations in Hes7 and G1-S transition with a period of roughly 2.5 hr (Fig.
189 2H,I, Movie S3). This suggested that in this region one cell after the other
190 showed high expression of the Fucci2-Cdt1 reporter. This in turn implied that
191 neighbouring cells were shifted in their G1-S transition by n x segmentation
192 clock period relative to their neighbours (Fig. 2J).
193 Thus, cell cycle progression is correlated with the segmentation clock
194 and has a constant phase-relationship with Wnt-signalling oscillations along the
195 AP axis of the PSM.
196
197 **Segmentation clock and cell proliferation are coupled**
198 We next sought to determine whether cell proliferation is merely
199 correlated to the segmentation clock or whether there is a functional link
200 between the two. Continuous inhibition of Wnt signalling by genetic or chemical
201 perturbation leads to impaired PSM growth and a rapid regression of the PSM
202 due to accelerated differentiation and loss of the morphogen gradient[30,31] (Fig.

203 S8). Such continuous perturbations are therefore not ideally suited to reveal a
204 functional relationship between two oscillators. Therefore, we needed a system
205 to subtly modulate oscillations. To achieve this, we used our previously
206 established microfluidic system to entrain oscillations to external pulses of
207 pathway modulation[29,32]. We cultured embryonic tail tips in Fibronectin-coated
208 microfluidic chips, so that the embryonic tissue spreads in a "quasi-monolayer"
209 and the embryonic axis is re-organized from posterior-anterior to centre-
210 periphery[6,29]. This arrangement in combination with mosaic labelling allows for
211 single-cell tracking even in standard confocal microscopes[20]. Using embryos
212 expressing Achilles-Hes7, inducible Fucci2-Cdt1 and iRFPnucmem[19,25,33], we
213 then addressed whether there was a functional link between proliferation and
214 the segmentation clock. Importantly, the correlation between Hes7 oscillations
215 and G1-S transition at population level was maintained in these cultures (Fig.
216 S9, Movie S4).

217 We modulated the segmentation clock by periodically perturbing Wnt
218 signalling using the GSK3 inhibitor Chiron (CHIR99021) (Fig. 3A, Movies S5-
219 S9). Our previous experiments had revealed that Chiron efficiently entrains
220 Wnt-signalling oscillations, which also affects Notch-signalling oscillations of
221 the segmentation clock[29]. Indeed, we confirmed that Chiron pulses entrained
222 the segmentation clock, using Achilles-Hes7 as a reporter (Fig. 3B-E).
223 Subsequently, we analysed when during one signalling oscillation cycle the
224 Fucci2-Cdt1 reporter peaked, corresponding to G1-S transition, and found that
225 G1-S transition preferentially occurred with the drug pulses (Fig. 3F-H, Fig.
226 S10). This is consistent with dynamics of the Wnt-signalling reporter Axin2T2A
227 that also peaked with the drug pulses[29]. In contrast, DMSO pulses led to a
228 random distribution of Fucci2-Cdt1 peaks during the oscillation cycle. This
229 indicates that modulating segmentation clock oscillations via targeted Wnt
230 signalling modulation entrains cell cycle oscillations.

231 All signalling pathways of the segmentation clock are known mitogens
232 promoting cells to enter the cell cycle. Recently, myc and Cyclin D, genes well
233 studied for their role in cell cycle progression and G1-S transition[26], have been
234 identified as potential cyclic genes at the mRNA level[3]. Indeed, using
235 hybridization chain reaction (HCR), we found Cyclin D1 to be expressed in the
236 PSM with a dynamic pattern overlapping with the Wnt-signalling target gene

237 Axin2 (Fig. 3I, Fig. S11A). Since cyclins are post-translationally regulated by
238 modulating protein stability, we stained for Cyclin D1 protein. This also showed
239 a corresponding staining pattern to Axin2 (Fig. 3J, Fig. S11B). To determine a
240 functional link, we perturbed Wnt signalling and analysed the effect on Cyclin
241 D expression. Since Wnt inhibition leads to an immediate loss of PSM due to
242 differentiation, we instead activated Wnt signalling using Chiron. This led to an
243 increase in Cyclin D expression in the entire PSM (Fig. 3K,L).
244 Thus, the segmentation clock and cell proliferation are coupled,
245 presumably via periodic induction of cell cycle regulators.
246
247 **An extended somitogenesis model suggests that cell cycle-**
248 **segmentation clock coupling ensures proper somite formation**
249 To determine whether the coupling of cell proliferation to signalling
250 oscillations had a functional role in maintaining periodic somite formation, we
251 turned to a conceptual modelling-based approach, extending on previous
252 models of somitogenesis[7,34-36]. Specifically, we modelled the dynamics of cells
253 in the PSM as a line of coupled Kuramoto-type phase oscillators and made the
254 following assumptions based on our findings and available literature: (1) At a
255 certain phase between Wnt- and Notch-signalling oscillations and a lower
256 threshold of the FGF morphogen gradient, somite formation occurs[29,37,38]. (2)
257 All PSM cells have a certain probability to divide, and the cell cycle period takes
258 values in the range 13.6 ± 1.3 hr (Fig. 1N). (3) Since FGF mRNA is known to
259 only be produced in the posterior tailbud[38,39], the FGF morphogen gradient is
260 diluted by mRNA degradation as well as cell division, when the mRNA present
261 in a cell is partitioned equally into the two daughter cells. (4) Minimal
262 rearrangement of cells in the one-dimensional model of the PSM was allowed.
263 This assumption was consistent with quantifications of cell migration and
264 rearrangement in the PSM cells tracked using light-sheet imaging (Fig. 4A-D,
265 Fig. S12A,B). While cells in the tailbud moved constantly (Movie S1), the
266 movement of cells in the PSM were much more restricted (0.1 μm/ 15 min) with
267 cells moving relative position by less than one cell diameter over the period of
268 the segmentation clock cycle (Fig. 4C). (5) We imposed the condition that cell
269 division occurs 1.25 ± hr after Wnt oscillations peak (Fig 2D). Based on these
270 assumptions, numerical simulations of this minimal one-dimensional model

271 recapitulated features of the continuously growing PSM field, with periodic
272 formation of somites (Supplemental discussion).
273 Based on our finding that cell proliferation occurs along the entire PSM,
274 we first questioned what effect the coupling of cell cycle entry with the
275 segmentation clock has. To this end, we considered a line of 50 cell grid points,
276 each containing 10 cells, based on the number of cells in a line from posterior
277 to anterior PSM and minimal cell exchange with neighbours (Fig. S12C and Fig.
278 4A-C), and simulated tissue growth and somite formation (Fig. 4E, Fig. S13).
279 Assuming that cell divisions occur randomly, decoupled from the segmentation
280 clock, with a period of 13.6 ± 1.3 hr, numerical simulations revealed large
281 variations in somite size (Fig. 4E,F, CV = 0.31). Moreover, uncoupled growth
282 led to a non-uniform dilution of the FGF morphogen gradient (Fig. 4E, Fig.
283 S13A). In contrast, when the entry into cell cycle was coupled to the phase of
284 the segmentation clock, tissue growth and somite formation were more uniform
285 (Fig. 4G,H, Fig. S13,B CV = 0.20). This indicates that the coupling of cell
286 proliferation to the segmentation clock leads to uniform growth and uniform
287 dilution of the morphogen gradient regulating the spacing of somite formation.
288
289 **Perturbing cell proliferation interferes with morphogen gradient**
290 **dilution and scaling of somite formation**
291 To understand how cell proliferation affected the segmentation process,
292 we inhibited cell proliferation in 2D *ex vivo* cultures[6] of embryos expressing
293 Fucci2-Cdt1, Achilles-Hes7 and iRFPnucmem using different cell cycle
294 inhibitors. Inhibition resulted in the expected effects on Fucci2-Cdt1 levels and
295 an accumulation of non-dividing cells (Movie S10). Upon inhibition,
296 segmentation clock oscillations were maintained (Fig. S14A,B), as shown
297 previously[12]. This indicates that cell cycle progression is not a necessary driver
298 of segmentation clock oscillations[12].
299 To challenge the predictions of the model on the nature of somite
300 formation in the presence of cell proliferation, we inhibited proliferation in
301 growing embryo tails using Aphidicolin as strong continuous inhibitor (Fig. 5,
302 Movies S11, S12). This led to a decrease in cell number, as expected, but tissue
303 size remained largely unaltered due to continued cell growth, leading to a
304 decrease in overall cell density (Fig. S14C-G). We then quantified morphogen

305 gradients using as a readout Brachyury expression, which is directly affected
306 by FGF and Wnt3a gradients[39,40]. Consistent with the model, the Brachyury
307 gradient was expanded in the unsegmented PSM upon cell cycle inhibition (Fig.
308 5A-C). Similarly, the expression pattern of FGF8 and Axin2 mRNA were
309 expanded and less graded than in controls (Fig. S14H-K).

310 Consistent with the expansion of morphogen gradients[39], the size of the
311 oscillating field, a measure of the extent of differentiation, decreased less than
312 in control tails (Fig. 5D,E, Fig. S14L). Furthermore, we found that the phase
313 wave velocity did not decrease to the same extent as in control tissues but
314 remained higher, despite the decrease in cell number relative to control tissue
315 (Fig. S14L-M). This contrasted with unperturbed tissues, in which the wave
316 velocity slows with decreasing size and cell number[6]. This implies that the
317 relative phase-shift between oscillations in neighbouring cells decreases in the
318 absence of cell division.

319 Finally, we analysed the effect on somite formation. Aphidicolin
320 treatment led to the formation of disorganized somites with undiscernible
321 boundaries (Fig. 5F)[8]. The size of forming somites relative to PSM size was
322 affected with the ratio changing from 0.172 to 0.109, thereby indicating altered
323 scaling of somite formation (Fig. 5G-J). We note that since (a) cell density
324 between the PSM and somites (Fig. S14D-G) and (b) cell motility (Fig. 5K) were
325 comparable between control and cell cycle inhibition, this cannot account for
326 the effect on scaling.

327 Thus, cell cycle inhibition impairs somite formation and scaling of
328 somitogenesis.

329

330

331 **Discussion**

332 Here, we addressed the role of cell proliferation in somitogenesis,
333 showing a tight correlation between cell cycle entry and the π of the
334 segmentation clock. Further, we presented a mechanism by which the coupling
335 of cell division to the segmentation clock may ensure uniform PSM growth and
336 dilution of regulatory molecules, thereby modulating the scaling and uniformity
337 of somite formation.

338 In contrast to studies that support a posterior growth zone[41-43], we found
339 that cell proliferation was uniformly spread over the posterior and anterior
340 PSM[5,10]. Furthermore, cell proliferation was coupled to the segmentation clock,
341 likely via Wnt-induced expression of pro-proliferative factors such as Cyclin D[3],
342 which ensures uniform distribution of proliferating cells over the PSM. With a
343 proliferation rate of approximately 14 hr compared to a somitogenesis period of
344 2.7 hr, cell proliferation is a key component of mouse somitogenesis. Upon cell
345 cycle inhibition, cell division was abolished while tissue and cell growth
346 continued, indicating that cell division in the PSM has a negligible effect on
347 tissue growth within this timescale.
348 Morphogen gradients are generated by mRNA and protein production in
349 the posterior tip and levels slowly decrease as cells move down the posterior-
350 anterior axis of the PSM[38]. Thus, morphogen gradients are modified by mRNA
351 (and protein) degradation as well as cell division, which lead to a continuous
352 decrease in morphogen concentration and nuclear effector proteins in cells.
353 Indeed, inhibiting cell divisions expanded the morphogen gradients. In
354 agreement with the clock-and-wavefront model[36], regression of the oscillating
355 field was also reduced upon cell cycle inhibition. Moreover, signalling wave
356 velocity was increased and somite formation impaired. This suggests that the
357 principal role of cell division in the PSM may lie not in its contribution to tissue
358 growth but rather in shaping morphogen gradients for proper somite formation.
359 This is consistent with a model (Fig. 5L) in which cell divisions are
360 uniformly distributed over the tissue by coupling to the segmentation clock. This
361 leads to an increase in cell number uniformly distributed over the PSM, which
362 leads to (1) a uniform expansion of the oscillating field and (2) a uniform dilution
363 of morphogen mRNA and protein as well as downstream gradients. The
364 gradient affects wave dynamics[44] and both in turn regulate somite
365 formation[37,39]. Supported by mathematical modelling, this suggests that the
366 coupling of cell divisions to the segmentation clock ensures formation of
367 correctly sized somites. Scaling of segment size to PSM size has previously
368 been correlated with scaling of wave dynamics[6] or the FGF gradient[7] in mouse
369 and zebrafish, respectively, both of which we found to be affected by cell cycle
370 inhibition. Thus, this constitutes a mechanism by which local cell-intrinsic

371 regulations, i.e., whether to divide or not, is translated into tissue-wide
372 regulation of morphogenesis to ensure proper somite formation.
373 How our findings translate to other species remains to be addressed. In
374 zebrafish, continued tissue growth, impaired somite formation and decreased
375 cell density are observed in the PSM of *emi1* mutants, which stop proliferation
376 during gastrulation[8]. Moreover, segmentation clock oscillations correlate with
377 cell divisions in zebrafish[15], even though cell proliferation is thought to play a
378 minor role for tissue growth[45]. This could explain why in zebrafish segmentation
379 proceeds more quickly than growth and oscillation regression leading to a rapid
380 reduction of tissue size and a decrease in wave amplitude from 4π to 2π over
381 developmental time[35]. In human somitogenesis, a correlation between the
382 timepoint of cell division and Hes7 oscillations has not so far been observed[12].
383 To clarify the role of cell proliferation in human cells, cell cycle reporters specific
384 for the G1-S transition should be quantified in posterior or anterior PSM cells
385 relative to Hes7 oscillations.
386 Signalling oscillations have been observed in other tissue types and
387 developmental contexts. Correlations between such oscillations and cell
388 division have been described in several tissues (e.g., [46]). In *in vitro* cultures of
389 the small intestine, we recently identified Hes1 oscillations that also correlate
390 with cell divisions[47]. In neural stem cells interactions of Hes1 oscillations with
391 the cell cycle inhibitor p21 have been described[48]. Whether there is active
392 coupling in all of these examples and whether this has similar effects on growth,
393 differentiation and morphogenesis at the tissue level, as we identified here for
394 somitogenesis, are exciting questions for future research.
395

Figure Legends

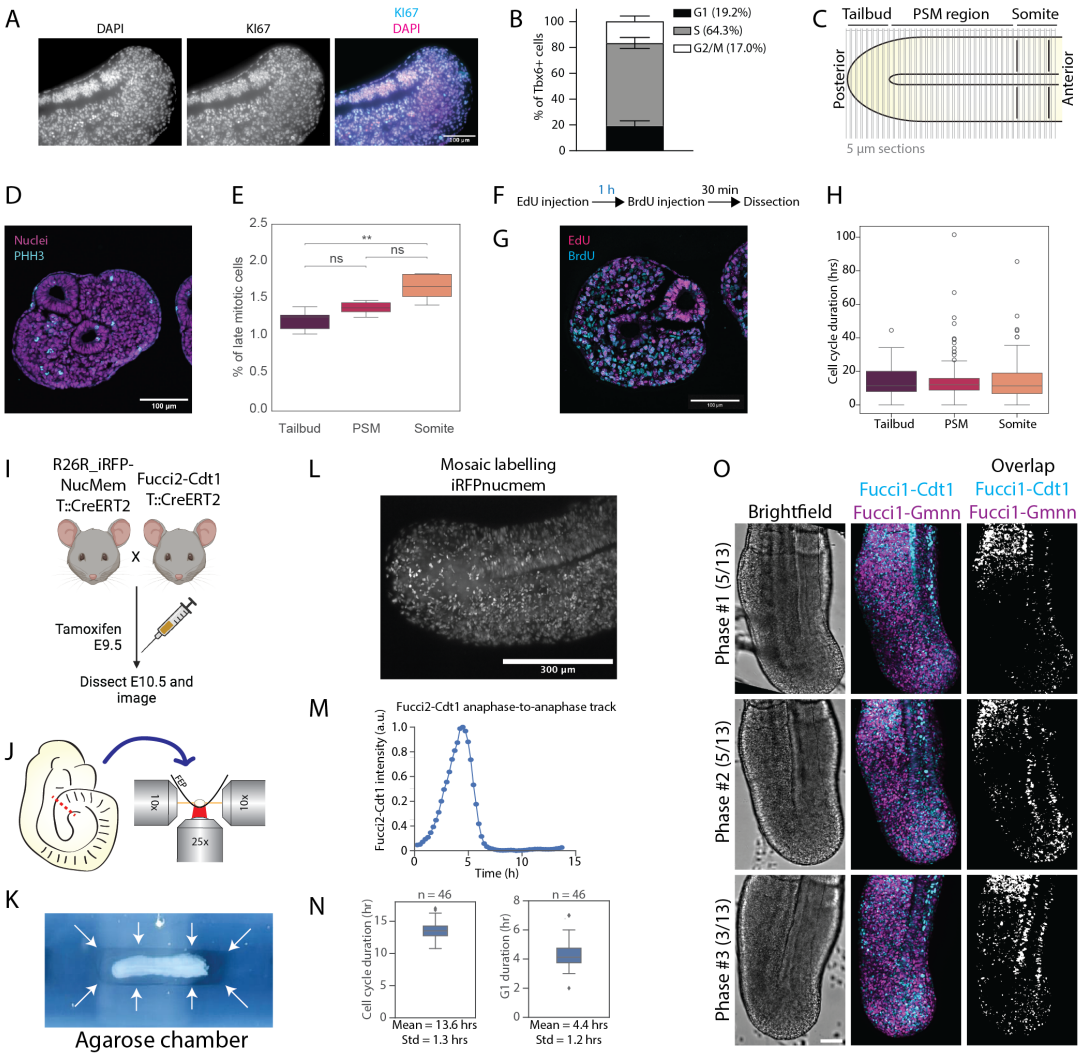

Figure 1 Cell cycle dynamics along the entire E10.5 presomitic mesoderm. **A-G** Quantification of cell cycle dynamics in uncultured tails. A 5 µm section of E10.5 tail with immunostaining for Ki67 and counterstaining with DAPI. **B** Flow cytometry analysis of embryonic tail cells stained for Tbx6 and DNA using Hoechst. DNA content in Tbx6-postive PSM cells. N=3 experiments. Raw data shown in Fig. S4. **C-E** Quantification of late mitotic cells in embryonic tails. N=5. **C** Embryonic tails were sectioned into 5 µm sections. Immunostaining against phosphorylated-histone H3 (PHH3) and counterstaining with DAPI were performed. For the analysis, tissue was divided into tailbud (posterior to neural tube), PSM and somite regions. **D** Representative image of a section stained against PHH3 and with DAPI (same as in Fig. S2A). **E** Quantification of cells in late mitosis (pro-metaphase to anaphase) in the regions indicated in **B**. **F-H** Quantification of cell cycle dynamics by EdU-BrdU double-labelling. N=3. **F**

411 Scheme of experimental setup. Embryos were dissected and tails sectioned
412 akin to **B** before EdU/BrdU staining. **G** Representative image of a section
413 stained for EdU, BrdU and nuclei (same as in Fig. S3A). **H** Quantification of cell
414 cycle length in the regions indicated in **B**. N = 3. **I-N** Quantification of cell cycle
415 dynamics in *ex vivo* cultured tails. **I** Pregnant mice were injected with low doses
416 of Tamoxifen on E9.5 for sparse nuclear labelling of cells. Embryos were
417 dissected after 24h of incubation. **J** Embryonic tails were dissected and imaged
418 with an inverted light-sheet microscope. **K** Brightfield image of tail within
419 agarose groove. **L** Representative image of embryonic tails with sparse-
420 labelling of nuclear marker iRFPnucmem. **M** Representative timeseries data of
421 the dynamics of the G1 marker Fucci2-Cdt1 in a single cell tracked from
422 anaphase to anaphase. **N** Quantification of cell cycle length and duration that
423 cells are positive for the G1 marker Fucci2-Cdt1. **O** Patterns of G1-S transition
424 in uncultured E10.5 embryonic tails (same as in Fig. S4F). Cells double-positive
425 for Fucci1-Cdt1 and Fucci1-Gem were determined in PSM of embryonic tails.
426 Tails were ordered into three phases according to their staining pattern: Phase
427 1: no double-positive cells in PSM; Phase 2: stripe of double-positive cells in
428 PSM; Phase 3: double-positive cells distributed over PSM. Number in brackets
429 indicates number of tails in which specific staining pattern was observed.
430 Brightfield (*left panel*), merge of Fucci1-Cdt1 and Fucci1-Gem (*middle panel*)
431 and cells double-positive for Fucci1-Cdt1 and Fucci1-Gem (*right panel*)
432 depicted. N=13. Scale bar 100 µm.
433
434

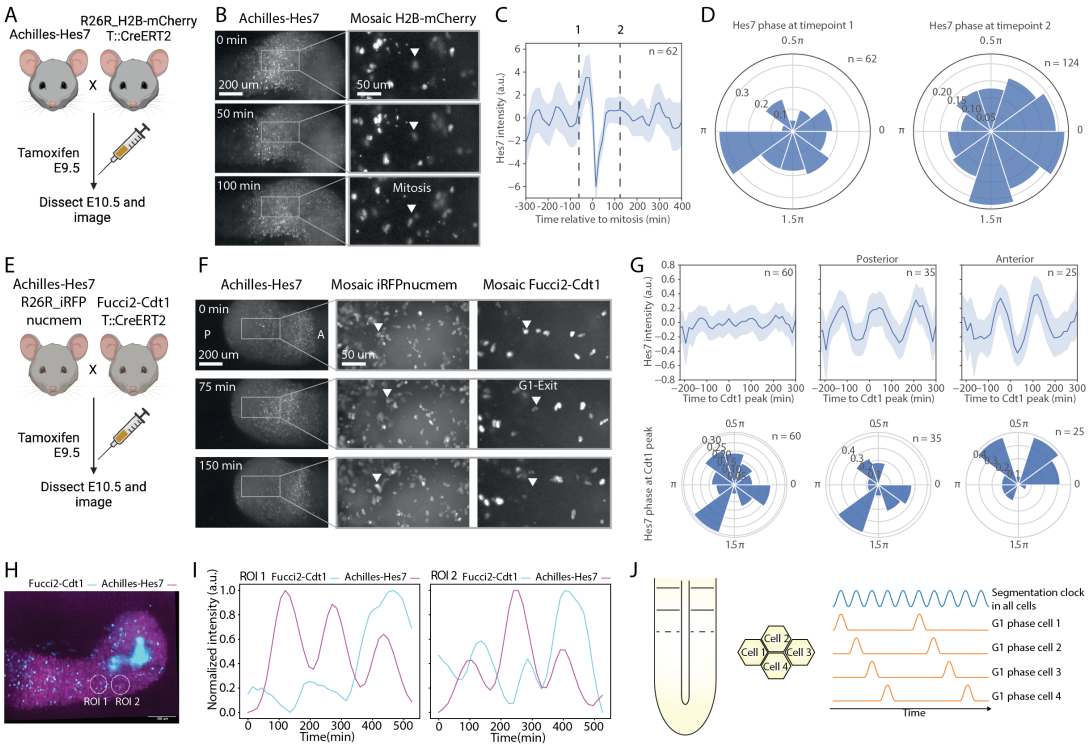

Figure 2 Cell cycle dynamics correlate with segmentation clock. A-D Correlation of Hes7 segmentation clock to cell division. **A** Experimental approach for sparse labelling of nuclei with H2B-mCherry combined with Achilles-Hes7. **B** Representative snapshots of timeseries data. Arrowhead points at one cell tracked over time. **C** Mean (blue line) and standard deviation (light blue shading) of Achilles-Hes7 signal of cells aligned to timepoint of cell division. **D** Phase of Achilles-Hes7 oscillations at timepoint 1, as indicated in **C**, (*left panel*) and at timepoint 2, as indicated in **C**, (*right panel*). **E-G** Correlation of Hes7 segmentation clock to G1-S transition. **E** Experimental approach for sparse labelling of nuclei with iRFPnucmem and Fucci2-Cdt1 combined with Achilles-Hes7. **F** Representative snapshots of timeseries data. Arrowhead points at one cell tracked over time. **G** Mean (blue line) and standard deviation (light blue shading) of Achilles-Hes7 signal of cells aligned to timepoint of G1-S transition. Left panel: all cells; middle panel: cells in posterior PSM; right panel: cells in anterior PSM. **H** Phase of Achilles-Hes7 oscillations at G1-S transition. Left panel: all cells; middle panel: cells in posterior PSM; right panel: cells in anterior PSM. **I** Maximum Intensity projection of E10.5 embryonic tail (purple: Achilles-Hes7, cyan: Fucci2-Cdt1). **J** Quantification of Achilles-Hes7 and Fucci2-Cdt1 in regions of interest (ROIs) as indicated in **I**. **K** Scheme

455 illustrating correlation of cell cycle (duration 13.6 hr) to segmentation clock
456 oscillations (2.7 hr).
457

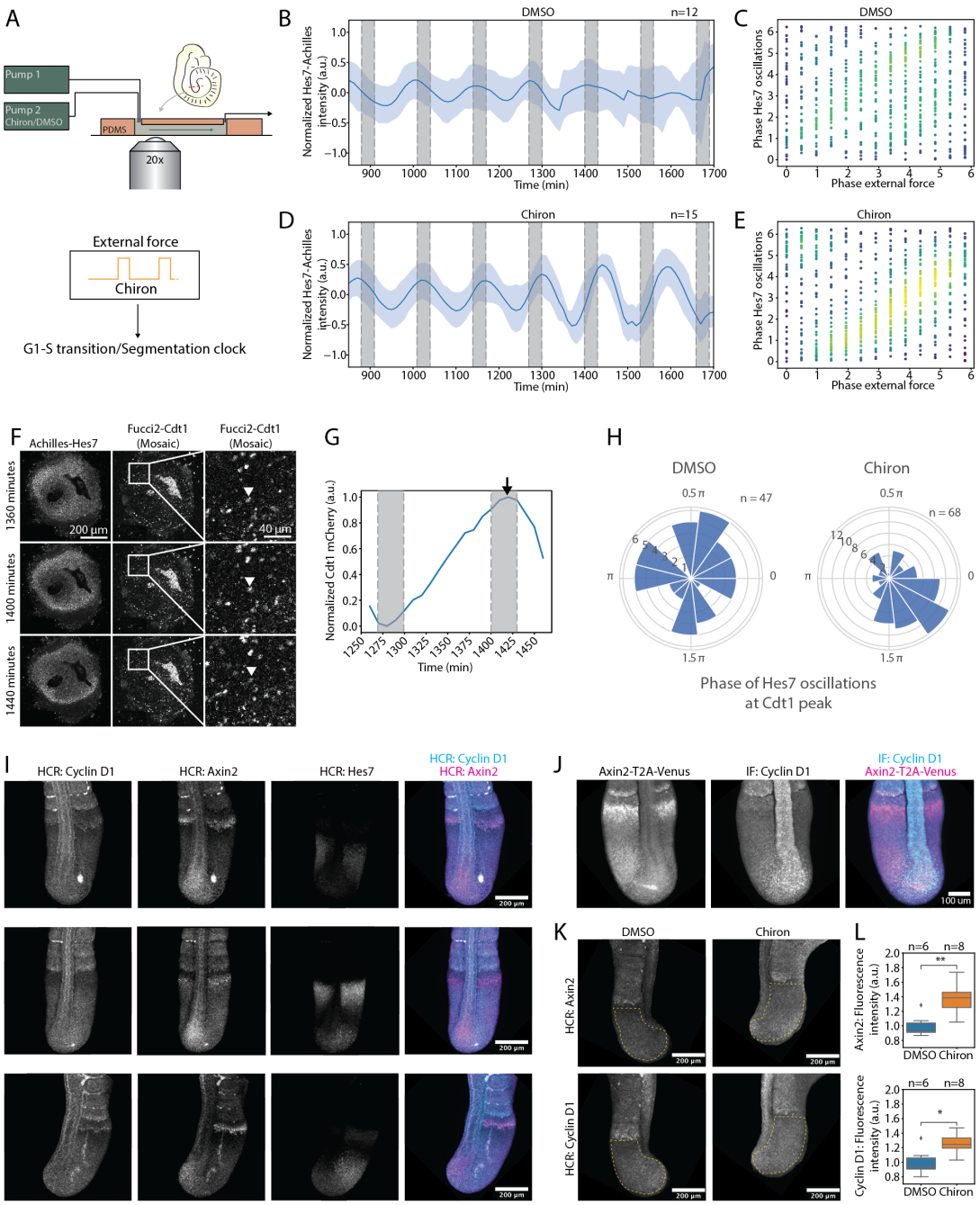

Figure 3 Coupling of cell proliferation to segmentation clock oscillations. A-H Microfluidics to test functional link. **A** Experimental approach: Microfluidic system to modulate segmentation clock oscillations in *ex vivo* tailbud cultures. Analysis of segmentation clock and cell proliferation. **B-E** Analysis of segmentation clock: **B,D** Mean (blue line) and standard deviation (light blue shading) of Achilles-Hes7 signal in anterior PSM upon treatment with DMSO (**B**) and 5 µM Chiron (**D**). **C,E** Phase of Hes7 oscillations plotted against phase of external drug pulses for treatment with DMSO (**C**) and 5 µM Chiron (**E**). **F** Snapshots of representative fluorescence real-time imaging data

468 highlighting tracking of a single cell (arrowhead). **G** Representative timeseries
469 data showing Fucci2-Cdt1 reporter intensity of a single cell during microfluidic
470 experiment. Grey shading indicates external drug pulse. **H** Phase of external
471 drug pulses, at which G1-S transition occurs in DMSO- (*left panel*) or Chiron-
472 treated samples (*right panel*). **I** Staining for mRNA levels of Axin2, Cyclin D1
473 and Hes7 in E10.5 embryonic tails using hybridization chain reaction (HCR)
474 (same as in Fig. S11A). **J** Immunostaining against Cyclin D1 in
475 Axin2T2AVenus-expressing E10.5 embryonic tails (same as in Fig. S11B). **K**
476 Treatment of E10.5 embryonic tails with DMSO or Chiron (10 μM). HCR for
477 Axin2 (upper panels) or Cyclin D1 (lower panels). Left panels: representative
478 images. Right panels: Quantification of Axin2 and Cyclin D1 in regions of
479 interest as indicated in representative images. * < 0.05; ** < 0.01.
480

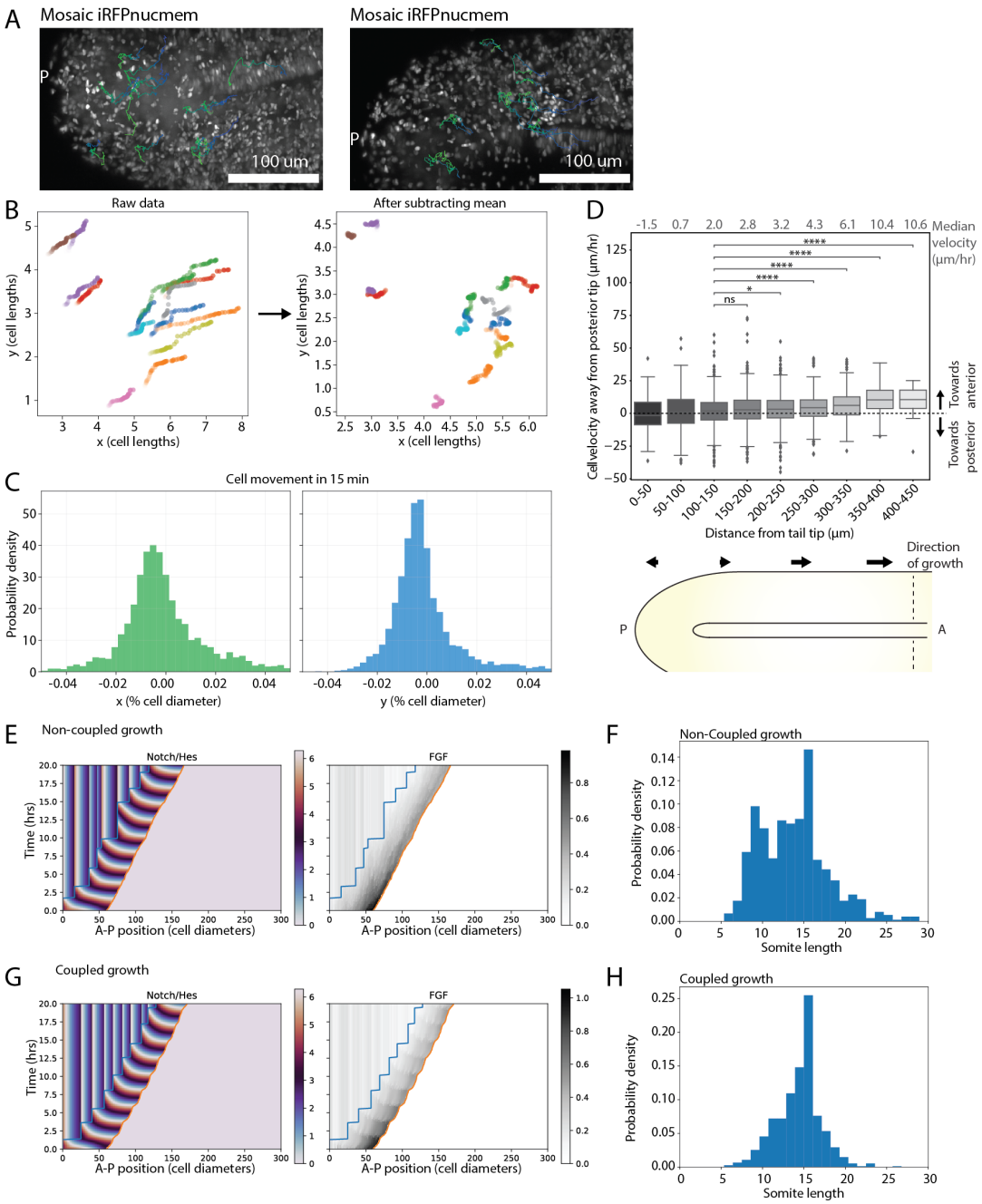

Figure 4 Uniform PSM growth and somite formation by coupling of cell proliferation to segmentation clock. A-D E10.5 embryonic tails were cultured ex vivo and fluorescence real-time imaging was performed (corresponds to data from Figure 1,2). **A** Snapshot of an embryonic tail imaged in a light-sheet microscope overlaid with tracks of single cells. **B** Plots of single cell tracks shown in A (*left panel*). Colours correspond to different cells. Each dot represents location of a cell at specific timepoint (interval between timepoints 15 min). Whole-tissue movement was computationally removed to reveal movement of single cells relative to their surrounding (*right panel*). **C**

Histogram of the amount of cell movement given in % of cell diameter (10 μm). N = 9 tissues n = 169 tracks. **D** Velocity of cells moving relative to the posterior tip (*top panel*). This indicates stretching of the PSM, as cells further away from the posterior have a higher velocity (*bottom panel*). Arrows indicate direction of movement. N = 6 tissues n = 106 tracks. * < 0.05; ** < 0.01; *** < 0.001; **** <0.0001. **E-H** Simulation of somitogenesis with random growth (E,F) or growth coupled to segmentation clock (G,H). **E,G** Example plots for simulations of signalling waves (*left panels*) as well as FGF gradient (gray shading) and somite formation (blue line) (*right panels*). **F,H** Histogram of somite lengths in 100 simulations. Coefficient of variation CV(random growth) = 0.31. CV(coupled growth) = 0.20.

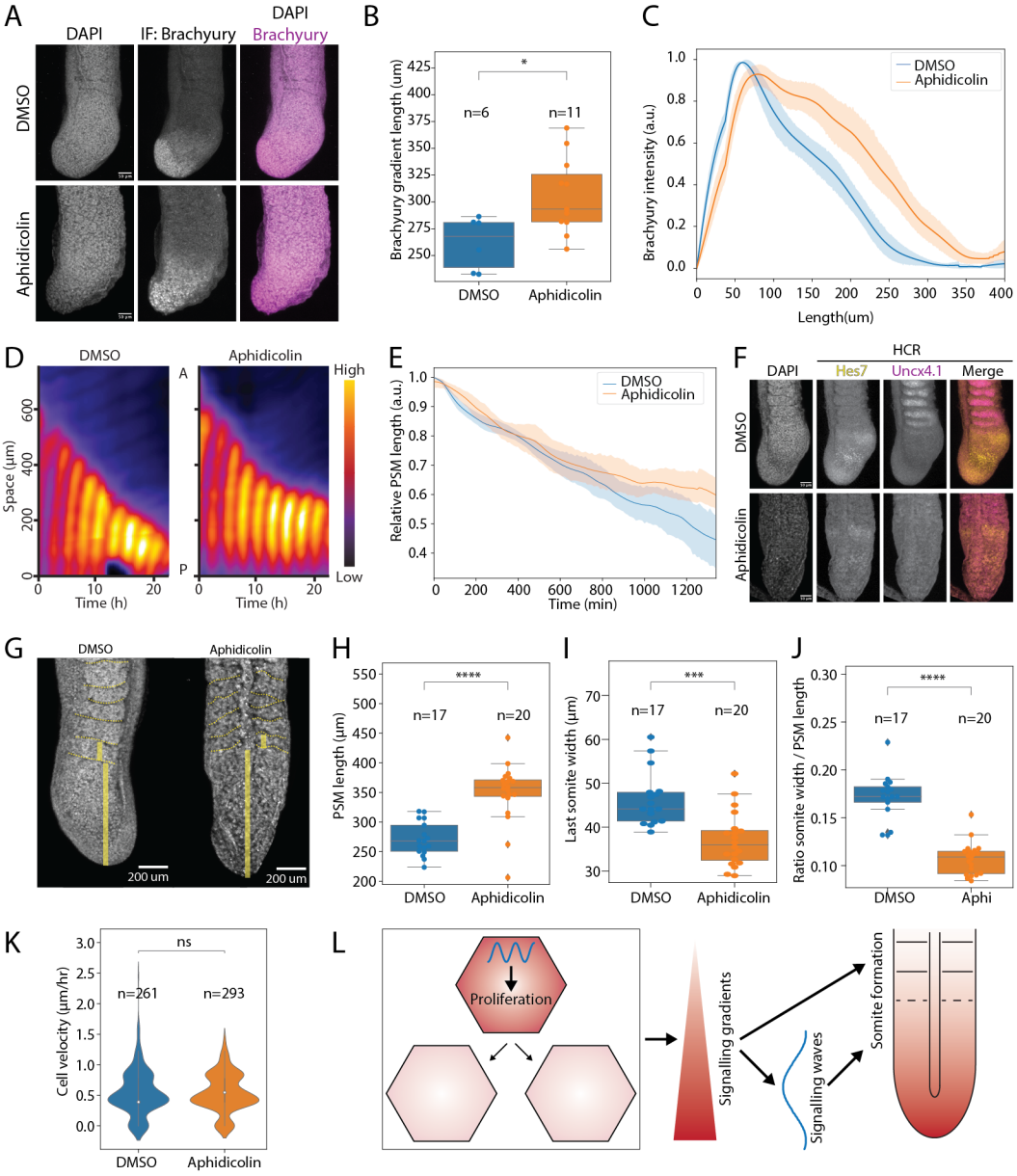

Figure 5 Coupling of cell cycle to segmentation clock affects scaling of somite formation. E10.5 embryonic tails were cultured *ex vivo* and treated with DMSO or the cell cycle inhibitor Aphidicolin. **A-C** After 23 hr of incubation, tails were fixed and stained for Brachyury and counterstained with DAPI. Scale bar 100 µm. **A** Representative images. **B** Quantification of the Brachyury signal along the AP axis of the PSM. Signal was normalized between 0 and 1. n(DMSO) = 6, n(Aphidicolin) = 11. **C** Quantification of the length of Brachyury gradient (Line: mean, shading: standard deviation). Intensity normalized between 0 and 1. * < 0.05; *** < 0.001; **** <0.0001. **D,E** Fluorescence real-time imaging of embryonic tails expressing Achilles-Hes7 was performed. **D** Representative kymographs of control and Aphidicolin-

treated samples. **E** Quantification of PSM length by determining the size of the oscillating field (Line: mean, shading: standard deviation). Length normalized to the PSM length at experiment start. n(DMSO) = 9, n(Aphidicolin) = 11? **F** After 23 hr of incubation, tails were fixed and HCR against Hes7 and Uncx4.1 as well as counterstaining with DAPI were performed. Representative images are shown (same as in Fig. S14J). **G-J** After 23 hr of incubation, tails were fixed and stained with DAPI. **G** Representative images are shown. **H-J** Quantification of PSM length from tail tip to last formed somite boundary (**H**), somite length (**I**) and the ratio of somite length to PSM length as a measure of scaling (**J**). **K** Quantification of cell motility in fluorescence real-time imaging data of embryonic tails expressing Achilles-Hes7 (data corresponds to D,E). **L** Schematic model of how coupling of cell proliferation to segmentation clock affects somitogenesis.

Methods

Animals and Housing

All experimental procedures were conducted in accordance with institutional guidelines and approved by the Ethical Review Board of the Hubrecht Institute. Animal protocols were reviewed and authorized by the Animal Experimentation Committee (DEC) of the Royal Netherlands Academy of Arts and Sciences. Mice were bred and housed under standard conditions at the Hubrecht animal facility, with a controlled environment maintained at 50–60% humidity, 22–23°C temperature, and a 12-hour light/dark cycle (inverted). Mice had ad libitum access to water and standard chow throughout the study.

Mouse Strains

All transgenic mouse lines used in this study have been previously described. The Achilles-Hes7 line was generously provided by the Kageyama laboratory[25]. Fucci [21], The R26R-H2B-mCherry, and R26R-mCherry-hCdt1(30/120)[24] lines were obtained from the RIKEN Center for Biosystems Dynamics Research and the RIKEN BioResource Research Center (accession numbers CDB0204K, RBRC02706, and CDB0229K, respectively) via the RIKEN Mouse Repository. The Tg(T-cre/ERT2)1Lwd/J ("T-CreERT2") line was sourced from The Jackson Laboratory (accession number #025520). The R26R-iRFPnucmem[20] and Axin-T2A-Venus[29] lines were provided by the Aulehla laboratory. All wild-type mice used in this study were F1 hybrids (BALB/cJ × C57BL/6J).

Animal and Embryo Work

EdU/BrdU Incorporation

Unless otherwise stated, female mice were sacrificed at 10.5 days post-coitum (dpc) and embryos were subsequently dissected. For EdU and BrdU incorporation experiments, pregnant females at 10.5 dpc were injected with 3.3 mg EdU in PBS, followed one hour later by an equimolar injection of 4.0 mg BrdU in PBS[49]. Mice were sacrificed 30 minutes after BrdU injection. Embryos were dissected in PBS supplemented with 1% Bovine Serum Albumin (Biowest, P6154) for tail extraction.

Sparse Labelling

565 For sparse labelling experiments, pregnant females were
566 intraperitoneally injected with tamoxifen (Sigma-Aldrich, T5648, dissolved in
567 corn oil) on embryonic day E9.5. To label with H2B-mCherry, 1 mg of tamoxifen
568 was administered, whereas for labelling with iRFPnucmem and Fucci reporters,
569 0.1 mg of tamoxifen was used.
570
571 Flow Cytometry
572 For flow cytometry analysis, E10.5 mouse tails were extracted and cut
573 into smaller pieces using a surgical scalpel to facilitate single-cell dissociation.
574 Tail fragments were washed three times in PBS0 in Eppendorf tubes, followed
575 by a 15-minute incubation with 400 µl of TrypLE (Thermo Fisher, 12604013).
576 After incubation, the tissue was passed through a 30G needle to generate a
577 single-cell suspension. The suspension was then washed twice in PBS0
578 supplemented with 1% Bovine Serum Albumin (Biowest, P6154) by
579 centrifugation at 500 g for 5 minutes.
580 To fix the cells, the pellet was resuspended in 4% paraformaldehyde
581 (PFA) and incubated at room temperature for 15 minutes. After two additional
582 washes in PBS with 1% BSA, cells were stored at 4°C until further staining. For
583 immunofluorescent staining, the single-cell pellet was resuspended in 3% BSA
584 PBS with 0.25% Triton X-100 and incubated overnight at 4°C with anti-Tbx6
585 rabbit primary antibody (Abcam, ab38883) at a dilution of 1:1000. After three
586 washes in 3% BSA PBS, the cells were incubated with secondary donkey anti-
587 rabbit Alexa Fluor 488 antibody (Thermo Fisher, A-21206) at a dilution of
588 1:1000 for 2 hours at room temperature.
589 Following a further two washes, the single-cell suspension was
590 resuspended in 500 µl of PBS supplemented with Hoechst 34580 (1 µg/ml) and
591 passed through a 20 µm mesh. Flow cytometry was performed on a CytoFLEX
592 S Flow Cytometer, and the Tbx6-positive cell population was selected for cell
593 cycle analysis using FlowJo software.
594
595 Culture of Live Embryonic Tissue
596 Culture of whole mount and spread-out tail tip tissues was performed as
597 previously described[29]. For perturbation experiments on whole mount and
598 spread-out tail tips, the following compounds were used: CHIR99021 (Chiron,

599 Sigma-Aldrich, SML1046) at 10 μM, IWP-2 (Sigma-Aldrich, I0536) at 1 μM,
600 Aphidicolin (ThermoFisher, J60236.MCR) at 1.6 μg/mL, Thymidine (Sigma-
601 Aldrich, T9250) at 2 mM, Palbociclib (Selleckchem, PD-0332991) at 1 μM, and
602 RO-3306 (Sigma-Aldrich, 217699) at 10 μM.
603
604 Microfluidics Experiment
605 The full protocol for performing the microfluidics experiment has been
606 described elsewhere[29,32]. For entrainment of Achilles-Hes7 and Fucci2-Cdt1
607 reporter lines, a pulsing scheme was employed consisting of 100 minutes of
608 medium followed by 30 minutes of medium containing CHIR99021 (Chiron,
609 Sigma-Aldrich, SML1046) at 5 μM or DMSO.
610
611 Confocal Live Imaging
612 Confocal live imaging was performed using a Leica TCS SP8 confocal
613 microscope equipped with a HC PL APO CS2 20×/0.75 DRY objective. For cell
614 tracking experiments, images were acquired every 10 minutes with a z-step of
615 5 μm, a stack depth of 50 μm, and a z-resolution of 4 μm. For non-tracking
616 imaging, images were taken every 10 minutes with a z-step of 10 μm, a stack
617 depth of 100–150 μm, and a z-resolution of 9 μm. Excitation of Achilles,
618 mCherry, or iRFP signals was performed using OPSL lasers at 514 nm, 568
619 nm, or 638 nm, respectively. Movies were recorded at a resolution of 512 × 512
620 pixels (pixel size 1.517 μm).
621
622 Light-sheet Live Imaging
623 Live imaging of whole mount embryo tails for single-cell analysis was
624 performed using a Viventis light sheet microscope (Viventis Microscopy, #LS1
625 Live). Imaging was conducted in a humidified atmosphere maintained at 37°C,
626 with 5% CO_2 and 60% O_2. For fluorescence excitation, lasers with wavelengths
627 of 514 nm, 568 nm, and 687 nm were used for Achilles, mCherry, and iRFP,
628 respectively. Imaging was carried out with a 25× objective, using a laser beam
629 of 3.3 μm and acquiring a z-stack of 60 steps, each with a 3 μm increment.
630 Images were captured at a resolution of 2048 × 2048 pixels every 15 minutes.
631 To prevent whole mount tissues from moving out of the field of view while still
632 allowing unperturbed growth, a 2% agarose gel in PBS was cast around a

633 custom-made insert in the sample holder. This insert created four spaces (1.5
634 mm × 0.5 mm) for the individual tissues to be loaded.
635
636 Paraffin Sectioning of Tissues and Immunofluorescence
637 Tissues fixed overnight in 4% paraformaldehyde (PFA) at 4°C were
638 stored in 70% ethanol at 4°C for up to one week prior to embedding. Embryo
639 tails were then subjected to Xylene treatment, embedded in paraffin in groups
640 of three, and sectioned transversally into 5 μm thick slices.
641 For staining, the slides were sequentially immersed in Xylene, followed
642 by 100%, 95%, 70%, and 50% ethanol, and rinsed with running cold tap water
643 for 3 minutes each. Antigen retrieval was performed by heating the slides in a
644 citrate buffer (8.2 mM sodium citrate and 1.8 mM citric acid, pH 6). Slides were
645 blocked and permeabilized using 1% Bovine Serum Albumin (BSA, Biowest,
646 P6154) in 0.5% Triton X-100 PBS. Mitotic cells were stained with anti-phospho-
647 histone H3 (Sigma-Aldrich, 05-806) at a 1:1000 dilution in 1% BSA PBS, and
648 incubation was carried out overnight at 4°C. Secondary staining was performed
649 using Donkey anti-Mouse Alexa Fluor 488 (Thermo Fisher, A-21202) at a
650 1:1000 dilution, supplemented with DAPI (5 μg/mL, Sigma) in 1% BSA PBS,
651 and incubation was carried out overnight at 4°C. After staining, slides were
652 mounted with Vectashield (H1200NB, Vector Laboratories). Images were
653 acquired using a Leica TCS SP8 confocal microscope with an HC PL APO CS2
654 20×/0.75 DRY objective and OPSL lasers at 365 nm and 488 nm for excitation.
655 For BrdU and EdU staining, two additional steps were incorporated. Prior
656 to blocking and after antigen retrieval, slides were incubated at room
657 temperature in 2 M HCl for 10 minutes. EdU was then visualized using the Alexa
658 Fluor™ 647 dye from the Click-iT™ EdU Cell Proliferation Kit for Imaging
659 (Thermo Fisher, C10340). BrdU was detected using an anti-BrdU antibody
660 (Thermo Fisher, B35128) at a 1:500 dilution, followed by secondary staining
661 with Donkey anti-Mouse Alexa Fluor 568 (Thermo Fisher, A10037).
662
663 Whole Mount Tissue Antibody Staining
664 Prior to immunostaining, samples were fixed overnight in 4%
665 formaldehyde at 4°C and stored in PBS at 4°C. Primary antibodies used for
666 staining included anti-Ki67 (Abcam, ab16667) at 1:1000, anti-T (human/mouse)

667 (R&D Systems, AF2085-SP) at 1:1000, and anti-Cyclin D1 (Cell Signaling,
668 2978) at 1:500. Secondary antibodies included Donkey anti-Goat Alexa Fluor
669 488 (Thermo Fisher, A-11055) at 1:1000 and Donkey anti-Rabbit Alexa Fluor
670 568 (Thermo Fisher, A10037) at 1:1000.
671 Immunostaining was carried out by incubating the samples with primary
672 and secondary antibodies overnight in PBST (0.1% Triton X-100) containing
673 1% Bovine Serum Albumin (BSA, Biowest, P6154). The secondary antibody
674 mixture was supplemented with DAPI (Sigma, 5 µg/mL) for nuclear staining.
675 For imaging, a z-stack consisting of 10-12 planes with a 10 µm distance
676 between each plane was acquired at a resolution of 1024 × 1024 pixels (pixel
677 size 0.758 µm) using a Leica TCS SP8 MP confocal microscope with a HC PL
678 APO CS2 20×/0.75 DRY objective. Excitation was performed with OPSL lasers
679 at 365 nm, 488 nm, and 568 nm.
680
681 Whole Mount Tissue Hybridization Chain Reaction (HCR)
682 Hybridization chain reaction (HCR) was performed as described
683 previously[50]. Cyclin D1 and Fgf8 probe sets were generated using an online
684 probe generator (https://github.com/rwnull/insitu_probe_generator). Probe sets
685 for Axin2, Hes7, and Uncx4.1 were obtained from Molecular Instruments. HCR
686 imaging was performed using a Leica TCS SP8 confocal microscope with a HC
687 PL APO CS2 20×/0.75 DRY objective. The system was equipped with OPSL
688 lasers for excitation at 365 nm, 488 nm, 568 nm, and 638 nm.
689
690 Image and Data Processing
691 To quantify the fraction of phospho-histone H3 (pHH3)-positive cells,
692 skin, neural tube, notochord, and gut were manually removed from the DAPI
693 channel in section images using Fiji. Subsequently, StarDist, a Fiji plugin, was
694 used to segment the remaining nuclei, providing an accurate measurement of
695 the number of nuclei per slice. pHH3-positive cells were manually counted per
696 slice.
697 For the quantification of EdU- and BrdU-positive cells, skin, neural tube,
698 notochord, and gut were similarly excluded from the DAPI channel in Fiji. This
699 channel was further denoised using Remove Outliers in Fiji (pixel size= 4,
700 threshold=50) followed by a gaussian blur with a sigma of 2. Using Cellpose

701 cryo3 model we segmented the remaining nuclei, allowing for an accurate count
702 of the total number of nuclei per slice. Mean intensities of EdU and BrdU were
703 calculated within the DAPI masks, and thresholds were applied to categorize
704 cells as positive or negative for EdU and/or BrdU. These annotations,
705 expressed as fractions of the total cell count, were used for the quantification
706 of cell cycle duration, population doubling time, and S-phase duration (see Fig.
707 1, Fig. S2,3).

708 To visualize tissue-wide dynamics of Hes7 and Fucci2-Cdt1, regions of
709 interest (ROIs) were drawn in maximum intensity projections of time-lapse
710 movies in Fiji. Intensity measurements of both channels were quantified over
711 time, smoothed, and linearly normalized between 0 and 1. Kymographs of
712 tissue-wide dynamics were generated using the KymoResliceWide plugin in
713 Fiji. A line was drawn from the posterior to the anterior end of the tissue, with a
714 width of 100 μm.

715 For the quantification of the T/Brachyury gradient, a similar approach
716 was used. A line plot was generated by measuring the intensity
717 of T/Brachyury along a line drawn in Fiji. Gradient length was defined as the
718 distance from the tip of the tail to the point where T/Brachyury intensity reached
719 10% above background level. To quantify staining intensities, an ROI was
720 manually drawn within the PSM, and the mean intensity was calculated using
721 Fiji. For the measurement of PSM and somite lengths, DAPI images were used.
722 Lines were drawn parallel to the neural tube from the tail tip to the first somite
723 boundary for PSM size, or from the first to the second somite boundary for
724 somite size.

725 For the quantification of tissue density, an ROI was drawn within confocal
726 or light sheet images, and the number of cells within the selected area was
727 counted using either the Achilles-Hes7 or DAPI channel.

728 To track single cells over short time intervals in confocal microscopy
729 movies, an ROI of 3 × 3 pixels was manually tracked within the Fucci2-
730 Cdt1 or Achilles-Hes7 channel in Fiji. The peak intensity of Fucci2-Cdt1 was
731 defined as the moment when a cell transitions from G1 to the S-G2-M phase.
732 These tracks were used to quantify cell velocity or the timing of cell cycle
733 transitions.

For long-term single-cell tracking in light sheet images, cells were manually tracked by following mosaically expressed H2B or Nucmem reporters using the Fiji plugin Mastodon (https://github.com/mastodon-sc/mastodon). Spot centre intensities were measured within the tracked spots to quantify Achilles-Hes7 or Fucci2-Cdt1. These intensities were smoothed using a moving average of 3 time points and linearly normalized, such that each track contained intensity values between 0 and 1. For the analysis of Hes7 dynamics, PyBOAT was used with the following settings: min_period = 60 min, max_period = 300 min, and TC = 150. All data plotting was performed using Python.

Statistical Analysis

All experiments were conducted with a minimum of three independent replicates. Data visualization was performed using Tukey-style boxplots, where the bar represents the median, the box delineates the 25th and 75th percentiles, and the whiskers extend to 1.5 times the interquartile range (IQR). Violin plots were used to display the distribution of data from the maximum to the minimum, with the bar indicating the median value. For statistical comparisons between groups, normality was assessed using the Shapiro-Wilk test. Statistical significance was determined using either an independent t-test or the Mann-Whitney U test, depending on whether the data followed a normal distribution.

Data and Code availability

All data and custom code used in this study are available upon request to k.sonnen@hubrecht.eu.

Acknowledgements

We thank members of the Sonnen group for discussions and feedback. We are grateful to Takashi Hiiragi and Juan Garaycoechea for discussions. We thank Jan-Daniël de Leede for help with data analysis. We thank the animal, FACS and imaging facilities of the Hubrecht Institute for their support. We thank Alexander Aulehla for support and providing mouse lines, in particular the inducible iRFPnucmem line. The H2B-mCherry mouse line was kindly provided by the Riken Center for Biosystems Dynamics Research and the Fucci line by the Riken BioResource Research Center. The T-Cre/ERT2 line was kindly provided by Jackson Laboratories. The Achilles-Hes7 was kindly provided by Ryoichiro Kageyama. This work was supported by the Hubrecht Institute and received funding from the European Research Council under an ERC starting grant agreement no. 850554 to K.F.S. In addition, this research was supported in part by grant NSF PHY-1748958 to the Kavli Institute for Theoretical Physics (KITP).

Author Contributions

M.J.O. and K.F.S. conceived the project together with Y.I.L. and B.D.S.; K.F.S. supervised the project; M.J.O. performed experiments with help from W.H.M.M., T.N., C.F., E.T., J.K. and W.M.T.; M.J.O., Y.I.L. and K.F.S. analysed the data; Y.I.L. and B.D.S. developed the theoretical framework; M.J.O., Y.I.L. and K.F.S. wrote the manuscript with input from all authors.

References

1 Meijer, W. H. M. & Sonnen, K. F. From signalling oscillations to somite formation. *Current Opinion in Systems Biology* **39**, 100520 (2024). https://doi.org/https://doi.org/10.1016/j.coisb.2024.100520

2 Hubaud, A. & Pourquie, O. Signalling dynamics in vertebrate segmentation. *Nat Rev Mol Cell Biol* **15**, 709-721 (2014). https://doi.org/10.1038/nrm3891

3 Matsuda, M. *et al.* Recapitulating the human segmentation clock with pluripotent stem cells. *Nature* **580**, 124-129 (2020). https://doi.org/10.1038/s41586-020-2144-9

4 Dequeant, M. L. *et al.* A complex oscillating network of signaling genes underlies the mouse segmentation clock. *Science* **314**, 1595-1598 (2006). https://doi.org/10.1126/science.1133141

5 Tam, P. P. The control of somitogenesis in mouse embryos. *J Embryol Exp Morphol* **65 Suppl**, 103-128 (1981).

6 Lauschke, V. M., Tsiairis, C. D., Francois, P. & Aulehla, A. Scaling of embryonic patterning based on phase-gradient encoding. *Nature* **493**, 101-105 (2013). https://doi.org/10.1038/nature11804

7 Ishimatsu, K. *et al.* Size-reduced embryos reveal a gradient scaling-based mechanism for zebrafish somite formation. *Development* **145** (2018). https://doi.org/10.1242/dev.161257

8 Zhang, L., Kendrick, C., Julich, D. & Holley, S. A. Cell cycle progression is required for zebrafish somite morphogenesis but not segmentation clock function. *Development* **135**, 2065-2070 (2008). https://doi.org/10.1242/dev.022673

9 Benazeraf, B. *et al.* Multi-scale quantification of tissue behavior during amniote embryo axis elongation. *Development* **144**, 4462-4472 (2017). https://doi.org/10.1242/dev.150557

10 Bulusu, V. *et al.* Spatiotemporal Analysis of a Glycolytic Activity Gradient Linked to Mouse Embryo Mesoderm Development. *Dev Cell* **40**, 331-341 e334 (2017). https://doi.org/10.1016/j.devcel.2017.01.015

11 Mongera, A., Michaut, A., Guillot, C., Xiong, F. & Pourquie, O. Mechanics of Anteroposterior Axis Formation in Vertebrates. *Annu Rev Cell Dev Biol* **35**, 259-283 (2019). https://doi.org/10.1146/annurev-cellbio-100818-125436

12 Diaz-Cuadros, M. *et al.* Metabolic regulation of species-specific developmental rates. *Nature* **613**, 550-557 (2023). https://doi.org/10.1038/s41586-022-05574-4

825 13 Diaz-Cuadros, M. *et al.* Metabolic regulation of species-specific
826 developmental rates. *bioRxiv*, 2021.2008.2027.457974 (2021).
827 https://doi.org/10.1101/2021.08.27.457974

828 14 Carrieri, F. A. *et al.* CDK1 and CDK2 regulate NICD1 turnover and the
829 periodicity of the segmentation clock. *EMBO Rep* **20**, e46436 (2019).
830 https://doi.org/10.15252/embr.201846436

831 15 Delaune, E. A., Francois, P., Shih, N. P. & Amacher, S. L. Single-cell-
832 resolution imaging of the impact of Notch signaling and mitosis on
833 segmentation clock dynamics. *Dev Cell* **23**, 995-1005 (2012).
834 https://doi.org/10.1016/j.devcel.2012.09.009

835 16 Wiedermann, G. *et al.* A balance of positive and negative regulators
836 determines the pace of the segmentation clock. *Elife* **4**, e05842 (2015).
837 https://doi.org/10.7554/eLife.05842

838 17 Kicheva, A. *et al.* Coordination of progenitor specification and growth in
839 mouse and chick spinal cord. *Science* **345**, 1254927 (2014).
840 https://doi.org/10.1126/science.1254927

841 18 Boehm, B. *et al.* The role of spatially controlled cell proliferation in limb
842 bud morphogenesis. *PLoS Biol* **8**, e1000420 (2010).
843 https://doi.org/10.1371/journal.pbio.1000420

844 19 Abe, T. *et al.* Visualization of cell cycle in mouse embryos with Fucci2
845 reporter directed by Rosa26 promoter. *Development* **140**, 237-246
846 (2013). https://doi.org/10.1242/dev.084111

847 20 El Azhar, Y. *et al.* Unravelling differential Hes1 dynamics during axis
848 elongation of mouse embryos through single-cell tracking. *Development*
849 **151** (2024). https://doi.org/10.1242/dev.202936

850 21 Sakaue-Sawano, A. *et al.* Visualizing spatiotemporal dynamics of
851 multicellular cell-cycle progression. *Cell* **132**, 487-498 (2008).
852 https://doi.org/10.1016/j.cell.2007.12.033

853 22 Palmeirim, I., Henrique, D., Ish-Horowicz, D. & Pourquie, O. Avian hairy
854 gene expression identifies a molecular clock linked to vertebrate
855 segmentation and somitogenesis. *Cell* **91**, 639-648 (1997).
856 https://doi.org/10.1016/s0092-8674(00)80451-1

857 23 Evrard, Y. A., Lun, Y., Aulehla, A., Gan, L. & Johnson, R. L. lunatic fringe
858 is an essential mediator of somite segmentation and patterning. *Nature*
859 **394**, 377-381 (1998). https://doi.org/10.1038/28632

860 24 Abe, T. *et al.* Establishment of conditional reporter mouse lines at
861 ROSA26 locus for live cell imaging. *Genesis* **49**, 579-590 (2011).
862 https://doi.org/10.1002/dvg.20753

25 Yoshioka-Kobayashi, K. *et al.* Coupling delay controls synchronized oscillation in the segmentation clock. *Nature* **580**, 119-123 (2020). https://doi.org/10.1038/s41586-019-1882-z

26 Morgan, D. O. *The cell cycle : principles of control*. (2007).

27 Tsiairis, C. D. & Aulehla, A. Self-Organization of Embryonic Genetic Oscillators into Spatiotemporal Wave Patterns. *Cell* **164**, 656-667 (2016). https://doi.org/10.1016/j.cell.2016.01.028

28 Meijer, H. A. *et al.* NOTCH1 S2513 is critical for the regulation of NICD levels impacting the segmentation clock in hiPSC-derived PSM cells and somitoids. *bioRxiv*, 2024.2012.2010.627712 (2024). https://doi.org/10.1101/2024.12.10.627712

29 Sonnen, K. F. *et al.* Modulation of Phase Shift between Wnt and Notch Signaling Oscillations Controls Mesoderm Segmentation. *Cell* **172**, 1079-1090 e1012 (2018). https://doi.org/10.1016/j.cell.2018.01.026

30 Aulehla, A. *et al.* Wnt3a plays a major role in the segmentation clock controlling somitogenesis. *Dev Cell* **4**, 395-406 (2003). https://doi.org/10.1016/s1534-5807(03)00055-8

31 Greco, T. L. *et al.* Analysis of the vestigial tail mutation demonstrates that Wnt-3a gene dosage regulates mouse axial development. *Genes & ,Ä¶* **10**, 313-324 (1996).

32 van Oostrom, M. J., Meijer, W. H. M. & Sonnen, K. F. A Microfluidics Approach for the Functional Investigation of Signaling Oscillations Governing Somitogenesis. *J Vis Exp* **169**, 1-17 (2021). https://doi.org/10.3791/62318

33 Masamizu, Y. *et al.* Real-time imaging of the somite segmentation clock: revelation of unstable oscillators in the individual presomitic mesoderm cells. *Proc Natl Acad Sci U S A* **103**, 1313-1318 (2006). https://doi.org/10.1073/pnas.0508658103

34 Pourquie, O. The segmentation clock: converting embryonic time into spatial pattern. *Science* **301**, 328-330 (2003). https://doi.org/10.1126/science.1085887

35 Soroldoni, D. *et al.* Genetic oscillations. A Doppler effect in embryonic pattern formation. *Science* **345**, 222-225 (2014). https://doi.org/10.1126/science.1253089

36 Cooke, J. & Zeeman, E. C. A clock and wavefront model for control of the number of repeated structures during animal morphogenesis. *J Theor Biol* **58**, 455-476 (1976). https://doi.org/10.1016/s0022-5193(76)80131-2

901 37 Niwa, Y. *et al.* Different types of oscillations in Notch and Fgf signaling
902 regulate the spatiotemporal periodicity of somitogenesis. *Genes Dev* **25**,
903 1115-1120 (2011). https://doi.org/10.1101/gad.2035311

904 38 Dubrulle, J. & Pourquie, O. fgf8 mRNA decay establishes a gradient that
905 couples axial elongation to patterning in the vertebrate embryo. *Nature*
906 **427**, 419-422 (2004). https://doi.org/10.1038/nature02216

907 39 Dubrulle, J., McGrew, M. J. & Pourquie, O. FGF signaling controls
908 somite boundary position and regulates segmentation clock control of
909 spatiotemporal Hox gene activation. *Cell* **106**, 219-232 (2001).
910 https://doi.org/10.1016/s0092-8674(01)00437-8

911 40 Naiche, L. A., Holder, N. & Lewandoski, M. FGF4 and FGF8 comprise
912 the wavefront activity that controls somitogenesis. *Proc Natl Acad Sci U*
913 *S A* **108**, 4018-4023 (2011). https://doi.org/10.1073/pnas.1007417108

914 41 Cambray, N. & Wilson, V. Axial progenitors with extensive potency are
915 localised to the mouse chordoneural hinge. *Development* **129**, 4855-
916 4866 (2002). https://doi.org/10.1242/dev.129.20.4855

917 42 Mathis, L. & Nicolas, J. F. Different clonal dispersion in the rostral and
918 caudal mouse central nervous system. *Development* **127**, 1277-1290
919 (2000). https://doi.org/10.1242/dev.127.6.1277

920 43 Neijts, R., Simmini, S., Giuliani, F., van Rooijen, C. & Deschamps, J.
921 Region-specific regulation of posterior axial elongation during vertebrate
922 embryogenesis. *Dev Dyn* **243**, 88-98 (2014).
923 https://doi.org/10.1002/dvdy.24027

924 44 Yaman, Y. I. & Ramanathan, S. Controlling human organoid symmetry
925 breaking reveals signaling gradients drive segmentation clock waves.
926 *Cell* **186**, 513-527 e519 (2023).
927 https://doi.org/10.1016/j.cell.2022.12.042

928 45 Thomson, L., Muresan, L. & Steventon, B. The zebrafish presomitic
929 mesoderm elongates through compaction-extension. *Cells Dev* **168**,
930 203748 (2021). https://doi.org/10.1016/j.cdev.2021.203748

931 46 Sabherwal, N. *et al.* Differential phase register of Hes1 oscillations with
932 mitoses underlies cell-cycle heterogeneity in ER(+) breast cancer cells.
933 *Proc Natl Acad Sci U S A* **118** (2021).
934 https://doi.org/10.1073/pnas.2113527118

935 47 Weterings, S. D. C. *et al.* NOTCH-driven oscillations control cell fate
936 decisions during intestinal homeostasis. *bioRxiv*,
937 2024.2008.2026.609553 (2024).
938 https://doi.org/10.1101/2024.08.26.609553

939 48 Maeda, Y., Isomura, A., Masaki, T. & Kageyama, R. Differential cell-
940 cycle control by oscillatory versus sustained Hes1 expression via p21.

941 *Cell Rep* **42**, 112520 (2023).
942 https://doi.org/10.1016/j.celrep.2023.112520

943 49 Zeng, C. *et al.* Evaluation of 5-ethynyl-2'-deoxyuridine staining as a
944 sensitive and reliable method for studying cell proliferation in the adult
945 nervous system. *Brain Res* **1319**, 21-32 (2010).
946 https://doi.org/10.1016/j.brainres.2009.12.092

947 50 Choi, H. M. T. *et al.* Third-generation in situ hybridization chain reaction:
948 multiplexed, quantitative, sensitive, versatile, robust. *Development* **145**
949 (2018). https://doi.org/10.1242/dev.165753
950

951